Experiments in Fluids (2024) 65:135
https://doi.org/10.1007/s00348-024-03873-2

RESEARCH ARTICLE

Pressure drop measurements over anisotropic porous substrates in channel flow

Shilpa Vijay[1,2] · **Mitul Luhar**[1]

Received: 22 March 2024 / Revised: 19 July 2024 / Accepted: 18 August 2024 / Published online: 31 August 2024

Abstract

Previous theoretical and simulation results indicate that anisotropic porous materials have the potential to reduce turbulent skin friction in wall-bounded flows. This study experimentally investigates the influence of anisotropy on the drag response of porous substrates. A family of anisotropic periodic lattices was manufactured using 3D printing. Rod spacing in different directions was varied systematically to achieve different ratios of streamwise, wall-normal, and spanwise bulk permeabilities (κ_{xx}, κ_{yy}, and κ_{zz}). The 3D printed materials were flush-mounted in a benchtop water channel. Pressure drop measurements were taken in the fully developed region of the flow to systematically characterize drag for materials with anisotropy ratios $\frac{\kappa_{xx}}{\kappa_{yy}} \in [0.035, 28.6]$. Results show that all materials lead to an increase in drag compared to the reference smooth wall case over the range of bulk Reynolds numbers tested ($\mathrm{Re}_b \in [500, 4000]$). However, the relative increase in drag is lower for streamwise-preferential materials. We estimate that the wall-normal permeability for all tested cases exceeded the threshold identified in previous literature ($\sqrt{\kappa_{yy}}^{+} > 0.4$) for the emergence of energetic spanwise rollers similar to Kelvin–Helmholtz vortices, which can increase drag. The results also indicate that porous walls exhibit a departure from laminar behavior at different values for bulk Reynolds numbers depending on the geometry.

✉ Mitul Luhar
luhar@usc.edu

Shilpa Vijay
shilpavi@usc.edu

[1] Department of Aerospace and Mechanical Engineering, University of Southern California, Los Angeles, California, USA

[2] Present Address: Center for Turbulence Research, Stanford University, Stanford, CA, USA

Graphical abstract

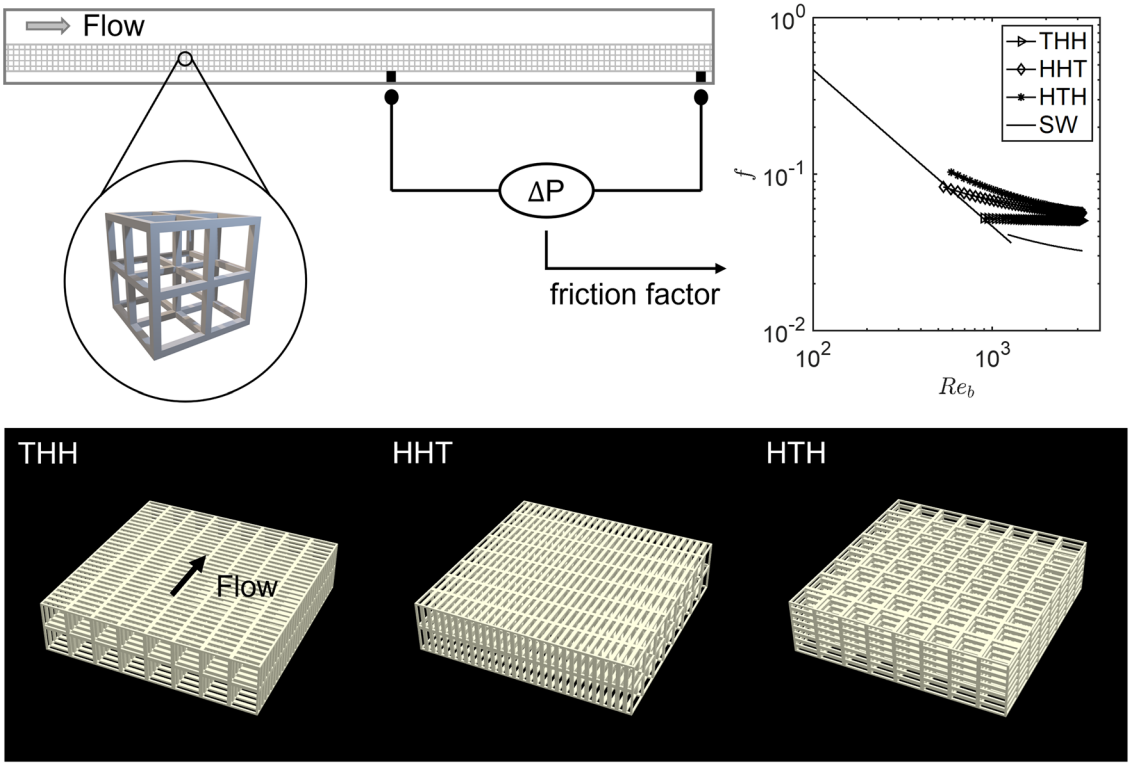

1 Introduction

Patterned and porous surfaces have shown significant promise as a method of passive turbulence control. For instance, streamwise aligned riblets have demonstrated drag reductions up to 10% in laboratory experiments (e.g., Walsh 1982; García-Mayoral and Jiménez 2011b). The underlying principle behind the drag-reducing effectiveness of riblets lies in their anisotropic nature: They offer significantly less resistance to the mean flow in the streamwise direction compared to turbulent cross-flows (Luchini et al. 1991). Within the grooves of riblets, the mean flow in the streamwise (x) direction experiences minimal impedance, resulting in a high interfacial slip. Conversely, cross-flows in the wall-normal (y) and spanwise (z) directions originating from turbulence are obstructed by the riblets and forced farther away from the wall. This obstruction effect weakens the quasi-streamwise vortices associated with the energetic near-wall (NW) cycle (Robinson 1991), consequently reducing turbulent mixing and momentum transfer above the riblets (Choi et al. 1993). More recent research by Garcia-Mayoral and Jimenez (García-Mayoral and Jiménez 2011a) has suggested that a Kelvin–Helmholtz (KH) instability can contribute to a decline in performance as riblet size increases, though not in all cases (Endrikat et al. 2021).

Recent theoretical and numerical simulations indicate that porous materials with streamwise-preferential anisotropy—substrates where the permeability is higher in the streamwise direction (κ_{xx}) as compared to the spanwise (κ_{zz}) and wall-normal (κ_{yy}) directions—have the potential to lower drag through a physical mechanism similar to that observed over riblets (García-Mayoral and Jiménez 2011a; Abderrahaman-Elena and García-Mayoral 2017; Gómez-De-Segura and García-Mayoral 2019). Simulation results predict that as much as 25% drag reduction can be achieved by using streamwise-preferential porous substrates (Gómez-De-Segura and García-Mayoral 2019).

Drag reduction over anisotropic permeable substrates can be explained using the virtual origin framework proposed by Luchini (1996). Within this framework, a streamwise slip length (ℓ_U^+) and a transverse slip length (ℓ_T^+) are defined to determine the virtual origin perceived by the mean flow and turbulent cross-flow below the porous surface, respectively. A superscript + denotes normalization with respect to the friction velocity u_τ and kinematic viscosity (ν). The virtual origin for the turbulent cross-flow can also be interpreted as the location where

the quasi-streamwise near-wall (NW) vortices perceive a non-slipping wall. Luchini (1996) suggested that the virtual origins of mean flow and turbulent cross-flow are set by the streamwise and spanwise velocities, $\ell_U^+ \approx \ell_x^+$ and $\ell_T^+ \approx \ell_z^+$, and that for small surface textures, drag reduction (DR) can be attributed to an offset between these virtual origins (Luchini 1996). This framework was generalized by Ibrahim et al. (2021), who further showed that the shift in the logarithmic region of the mean profile in wall-bounded flows is equal to the difference in virtual origins, $\Delta U^+ = \ell_U^+ - \ell_T^+$. Thus, surfaces that give rise to positive $\ell_U - \ell_T$ (or equivalently, $\ell_x - \ell_z > 0$) have the potential to yield an outward shift in the normalized mean profile, which is indicative of drag reduction.

Abderrahaman-Elena and García-Mayoral (2017) and Gómez-De-Segura and García-Mayoral (2019) extended the virtual origin framework to anisotropic permeable substrates and showed that streamwise and spanwise permeabilities can be related to the slip lengths as $\ell_x^+ \approx \sqrt{\kappa_{xx}}^+$ and $\ell_z^+ \approx \sqrt{\kappa_{zz}}^+$ for deep substrates, i.e., for $H^+ >> \ell_U^+$ where H is the thickness of the porous substrate. This implies $\Delta U^+ \propto \sqrt{\kappa_{xx}}^+ - \sqrt{\kappa_{zz}}^+$, or that drag reduction can be achieved with anisotropic materials with streamwise to spanwise anisotropy ratio, $\phi_{xz} = \kappa_{xx}/\kappa_{zz} > 1$. This is obtained by assuming that the idealized Darcy–Brinkman framework governs the flow generated within the porous layer in response to the overlaying shear. For small changes in friction, the drag reduction can be quantified as $\mathrm{DR} \approx \sqrt{2c_{f0}}\Delta U^+ \approx \sqrt{2c_{f0}}(\ell_U^+ - \ell_T^+)$, where c_{f0} is the smooth wall friction factor.

Although these models do not resolve the flow to the pore scale, they suggest that the drag reduction is achieved when the material is highly streamwise anisotropic in order to obtain a large $\sqrt{\kappa_{xx}}^+ - \sqrt{\kappa_{zz}}^+$. Linear stability analyses suggest that there is a limit to the drag-reducing capabilities of permeable surfaces. A deterioration in performance is typically observed when the normalized wall-normal permeability exceeds a certain threshold, $\sqrt{\kappa_{yy}}^+ \gtrsim 0.4$. This is thought to be due to the onset of a Kelvin–Helmholtz-type instability, which limits the maximum achievable drag reduction (Abderrahaman-Elena and García-Mayoral 2017; Gómez-De-Segura and García-Mayoral 2019). Thus, for drag reduction to be achieved, the material must exhibit streamwise-preferential slip as well as low wall-normal permeability.

Motivated by these findings, Habibi Khorasani et al. (2024) considered turbulent flows over porous lattices in scale-resolving direct numerical simulation (DNS). The porous substrates were designed with a repeating rectangular cubic cell pattern, a geometry that can be easily manufactured using additive techniques as demonstrated in previous experimental studies (Efstathiou and Luhar 2020; Chavarin et al. 2020). Due to resolution constraints, the substrates considered in DNS had relatively low volumetric porosity, $\epsilon \in [0.26, 0.75]$, and modest anisotropy ratios, $\phi_{xz} < 2$.

Habibi Khorasani et al. (2024) found that none of the substrates tested reduced drag compared to smooth wall conditions, despite several geometries exhibiting streamwise-preferential permeability. This is because high streamwise permeability is only beneficial for DR if it translates into high streamwise slip. While the Darcy–Brinkman framework predicts $\ell_U \propto \sqrt{k_{xx}}$, the specific geometry plays a central role in determining slip. The work of Abderrahaman-Elena and García-Mayoral (2017) and Gómez-De-Segura and García-Mayoral (2019) assumed that the porous materials comprised streamwise-oriented fibers with varying geometry and spatial density, for which the streamwise permeability and slip are expected to be correlated. In contrast, the geometries tested by Habibi Khorasani et al. (2024) consisted of intersecting rectangular rods oriented along the streamwise, wall-normal, and spanwise directions. Streamwise-preferential permeabilities were realized by increasing rod spacing in the wall-normal and spanwise directions (i.e., increasing pore size normal *perpendicular* to the streamwise flow) while limiting spacing in the streamwise direction. However, the small streamwise spacing led to an increase in the density of spanwise-oriented rods resulting in a decorrelation between streamwise permeability and slip. As a result, the DNS results did not show significant streamwise slip or drag reduction.

The DNS results did confirm a transition away from smooth-wall-like behavior due to the emergence of spanwise rollers beyond a threshold wall-normal permeability. The experiments presented in this paper test anisotropic porous materials with a similar geometry to those employed by Habibi Khorasani et al. (2024), albeit with higher porosity.

1.1 Previous experiments over anisotropic porous substrates

There are few experimental studies over a wide range of anisotropic porous materials, and fewer so in channel flow. As predicted, it has been observed for substrates with higher wall-normal permeability as compared to streamwise permeability that the emergence of Kelvin–Helmholtz-type rollers is possible and results in a substantial increase in drag (Suga et al. 2018; Chavarin et al. 2020; Morimoto et al. 2023). In experiments conducted by Suga et al. (2018), for the case with the lowest permeability, it was observed that although the flow is laminar at $\mathrm{Re}_b = 900$, from $\mathrm{Re}_b = 1300$ the mean velocity profile becomes asymmetric, indicating that transition to turbulence occurs in this interval. All other cases were tested at $\mathrm{Re}_b > 3400$ where the flow is already fully turbulent. Experiments for isotropic porous foams (Suga et al.

2010) similarly show an earlier departure from the laminar regime compared to smooth wall conditions.

In contrast to theoretical predictions, the limited experiments conducted thus far using streamwise-preferential porous materials do not show drag reduction compared to smooth walls (Chavarin et al. 2020). The small-scale experiments pursued by Chavarin et al. (2020) examined the effect of 3D printed porous materials with high streamwise permeability ($\kappa_{xx} > \kappa_{yy} = \kappa_{zz}$) as well as high wall-normal permeability ($\kappa_{xx} = \kappa_{zz} < \kappa_{yy}$) in partially porous channel flow at low friction Reynolds numbers, $\mathrm{Re}_\tau \approx 120$. The geometries tested comprised of a repeating cubic lattice, similar to the aforementioned DNS study by Habibi Khorasani et al. (2024). In the experiments, the material with higher streamwise permeability ($\sqrt{\kappa_{xx}}^+, \sqrt{\kappa_{yy}}^+, \sqrt{\kappa_{zz}}^+$) $\approx (8.2, 1.4, 1.4)$ did not show a significant difference from smooth wall conditions. However, the material exhibiting high wall-normal permeability showed a significant increase in drag. Similarly, Efstathiou and Luhar (2020) performed experiments on 3D printed materials with streamwise-preferential permeability ($\sqrt{\kappa_{xx}}^+ \approx 3.0$ and $\sqrt{\kappa_{yy}}^+ = \sqrt{\kappa_{zz}}^+ \approx 1.1$) on turbulent boundary layer flows at $\mathrm{Re}_\tau \approx 360$. For fully developed conditions, friction estimates show that the 3D printed porous substrate led to a small ($< 5\%$) increase in drag. Further, PIV-based measurements of turbulence statistics and velocity spectra indicate that the observed drag increase can potentially be attributed to the emergence of energetic spanwise rollers resembling Kelvin–Helmholtz vortices. For both these experiments, manufacturing limitations precluded the design of streamwise-preferential substrates with wall-normal permeabilities below the threshold identified for the emergence of spanwise rollers, $\sqrt{\kappa_{yy}}^+ < 0.4$ (Gómez-De-Segura and García-Mayoral 2019).

Recently, Morimoto et al. (2023) conducted channel flow experiments on substrates with high streamwise preference $\phi_{xz} > 6$ and $\sqrt{\kappa_{yy}}^+ \in [0.26, 0.69]$. However, no drag reduction was observed even for the substrates with wall-normal permeabilities below the threshold that gives rise to spanwise rollers. This lack of drag reduction was attributed to an increase in wall-normal velocity fluctuations. This again confirms that in addition to bulk properties such as permeability, the impact of anisotropic porous materials on turbulent flows also depends on the specific geometry. The substrates tested by Morimoto et al. (2023) comprised of stacked layers of corrugated and flat woven-wire meshes. The corrugations ensured high streamwise permeability. However, the interfacial layer comprised a flat wire mesh, which is likely to have limited the streamwise slip. Nevertheless, these prior studies indicate that $\sqrt{\kappa_{yy}}^+$ is a dominant scale governing drag increase.

In summary, prior experimental measurements for friction factors are limited to only a few ratios of anisotropy. Furthermore, friction estimates obtained in the previous experiments are also limited in the sense that friction velocity is not directly obtained from an independent measure, but inferred from other turbulence quantities such as mean velocity or Reynolds shear stress profiles. This limitation does not apply to prior numerical simulations. However, numerical simulations showing drag reduction have primarily made use of bulk models (e.g., permeability) to represent substrates and have been restricted to low to moderate Reynolds numbers, where the scale separation between outer and inner length scales might not be sufficient. To the best of the authors' knowledge, there has been no systematic study reporting friction factor values for anisotropic porous substrates in channel flow spanning a wide range of Reynolds numbers. There is also a dearth of data quantifying friction factor for anisotropic porous substrates in the transitional regime.

1.2 Contribution and outline

In this paper, we leverage a cubic unit cell microstructure to systematically design and manufacture anisotropic porous materials with varying streamwise, spanwise, and wall-normal permeability. We test these materials in a benchtop channel flow setup with direct pressure drop measurements, which can be used to estimate changes in drag. Due to fabrication constraints, the manufactured geometries did not yield permeability values in the range expected to generate drag reduction as per the simulations of Gómez-De-Segura and García-Mayoral (2019). Nevertheless, these measurements estimate the drag response for various values of anisotropy in conditions spanning both laminar and turbulent regimes. Since anisotropic materials have potential applications in enhancing heat transfer (Boomsma and Poulikakos 2002; Boomsma et al. 2003; Clyne et al. 2006) and mitigating aerodynamic noise (Jaworski and Peake 2013, 2020) while limiting the impact on drag, further research on anisotropic porous materials for drag reduction, thermal management, and noise control may benefit from a diagram akin to the Moody chart to predict friction factor and onset of transition. Such data can also provide insight into the choice of Re_b for future DNS simulations.

The remainder of this manuscript is structured as follows. Section 2 describes the experimental setup and introduces the porous lattices used for the experiment. The experimental procedure used to measure pressure drop as a function of bulk velocity across the test section and subsequently evaluate friction factors is also discussed in detail. In Sect. 3, the results are discussed including the smooth wall reference measurement, a comparison of the drag response for isotropic and anisotropic porous substrates, and observations on the departure from the laminar regime. Brief concluding remarks are presented in Sect. 4.

2 Experimental methods

2.1 Experimental setup

The aim of this experiment was to analyze the influence of substrate anisotropy on friction factor and to quantify the relative drag increase or decrease compared to smooth surfaces. For this, an asymmetric benchtop water channel setup was constructed where the test section allowed for porous substrates to be flush-mounted adjacent to an unobstructed flow. Similar channel configurations have been used in previous simulations (Breugem et al. 2006; Chandesris et al. 2013) and experiments (e.g., Suga et al. 2018; Chavarin et al. 2020; Morimoto et al. 2023). These studies show that the velocity distribution becomes asymmetric and deviates from the parabolic profile of the laminar case as Re_b increases. Under fully developed flow conditions, this setup can help discern the effects of the porous wall on near-wall turbulence compared to the smooth wall case. Moreover, the asymmetric setup allows for optical access to the unobstructed portion of the channel, potentially enabling future particle image velocimetry or laser Doppler velocimetry studies. The friction factor was characterized by measuring the pressure drop across the substrates in the fully developed region of the channel for a range of Reynolds numbers. A schematic of the experiment is shown in Fig. 1.

The benchtop channel was milled from acrylic and comprised an upstream flow conditioning section with flow straighteners and a 2:1 contraction to ensure uniform flow in the test section. The test section was created with a cutout of length $L = 700$ mm and depth $H_p = 6.35$ mm to accommodate porous substrates and ensure a flush interface with the upstream smooth wall. The width of the test section was $W = 80$ mm and the height of the unobstructed channel was $H_f = 6.35$ mm, providing an aspect ratio of $W/H_f \approx 12$. Seven pressure taps, each measuring 2 mm in diameter, were bored into the housing along the centerline, with the first pressure tap placed 94 mm from the test section entrance and subsequent pressure taps being 101 mm apart from each other. These pressure taps allowed the measurement of pressure drop at various locations in the test section to identify the region of the test section with fully developed flow, i.e., the region characterized by a linear decrease in pressure with distance. The pressure taps were included on the side of the channel with the cutout designed to house porous and smooth tiles. The smooth tiles had holes aligned with the pressure taps to avoid sheltering effects. We do not expect such sheltering effects to be important for the porous tiles since the materials tested in the experiments all have relatively high porosity ($\epsilon > 0.75$). As detailed below, pressure drop measurements were taken using a high-resolution *differential* pressure transducer (PX-409, Omega Inc.) for the fully developed region and converted into friction factor estimates.

Flow in the channel was generated using a submersible pump placed in a water tank. The volumetric flow rate was adjusted using a ball valve and measured with a washdown flowmeter (McMaster-Carr) with an accuracy of 2%. The volumetric flow rate varied from $\dot{V} = 50$ cm^3 s^{-1} to $\dot{V} = 250$ cm^3 s^{-1}. The bulk velocity was calculated

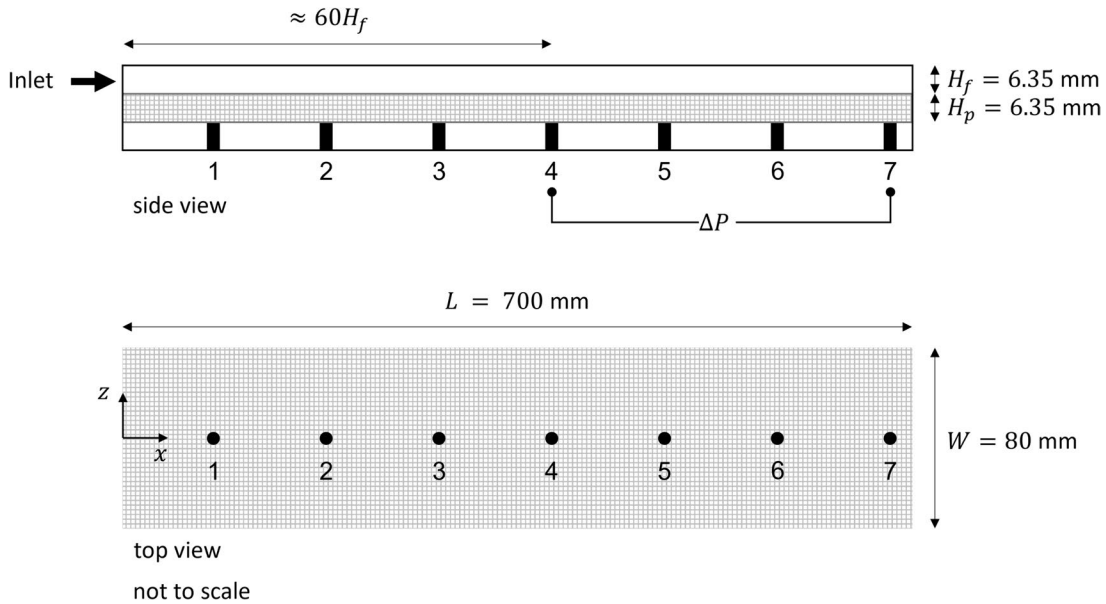

Fig. 1 Schematic side view and top view of the experimental setup (not to scale)

using the unobstructed channel height as $U_b = \dot{V}/(H_f W)$. This resulted in bulk Reynolds numbers in the range of $\mathrm{Re}_b = U_b H_f/\nu \in [500, 4000]$. These bulk Reynolds numbers span both laminar and turbulent flow conditions.

2.2 Porous substrates

A cubic lattice geometry similar to the one utilized by Chavarin et al. (2020) was used for the experiments. As shown in Fig. 2, the geometry comprised rods of a square cross section (side d) oriented along the streamwise (x), wall-normal (y), and spanwise (z) directions. To achieve geometries with varying anisotropy, the nominal rod spacing in the streamwise (s_x), wall-normal (s_y) and spanwise (s_z) directions was varied to create a family of anisotropic materials as shown in Table 1. Fabrication constraints (printing resolution, resin drainage) dictated the minimum rod spacing. Maximum spacing and pore size was limited by the maximum allowable overhang (or unsupported length) for the 3D printed parts before sagging was observed, causing the geometry to deviate from its designed dimensions.

The porous geometries were 3D printed using resin-based stereolithographic printers (Formlabs Form 3). The parameter space shown in Table 1 is considered in the lab experiments. Each 3D printed geometry is referenced using a three-letter combination that represents spacings in the x, y, and z dimensions. The letter H (High) corresponds to the largest spacing possible ($s = 3$ mm), M (Medium) and L (Low) correspond to intermediate spacings ($s = 2$ mm and $s = 1.5$ mm, respectively) and T (Tiny) corresponds to the lowest spacing possible ($s = 0.8$ mm) before individual pores started fusing. For example, a substrate with nominal spacings $(s_x, s_y, s_z) = (3, 1.5, 3)$ in mm is labeled as HLH. For all cases, the nominal rod size is kept constant at $d = 0.4$ mm.

The permeability of the porous lattice was measured experimentally. A custom-designed permeameter setup comprising a square duct that held 3D printed cubes of the porous material was developed. Each cube had a side length of 25 mm. To drive flow across the samples, a submersible pump placed in a larger reservoir was used, and the flow rate was regulated by an electronic proportioning valve (Omega PV14 series). The pressure drop across the sample was measured using a differential pressure transducer (Omega PX-409 series), and the permeabilities were calculated by fitting Darcy's law, including a Forchheimer correction term, to the velocity–pressure drop measurements. To estimate permeabilities in all directions, the cube was then rotated. Measured permeability values in all three directions are listed in Table 1.

Cases HHH, MMM, and LLL represent nominally isotropic materials with identical permeabilities in the x, y, and z directions. Cases MHH, LHH, and THH have smaller streamwise spacing as compared to wall-normal and spanwise spacing ($s_x < s_y = s_z$). This results in larger pore sizes for the streamwise flow as compared to the wall-normal and spanwise flow, and therefore yields materials with streamwise-preferential permeability. Cases THH, HTH, and HHT represent rotated versions of the same nominal microstructure.

We recognize that the specific geometry used here is likely to limit the interfacial slip velocity generated for streamwise-preferential materials (see Fig. 2d–f), thereby compromising drag reduction performance. Nevertheless, the present experiments are some of the first to systematically evaluate the effect of anisotropic porous substrates on drag across transitional and turbulent flow regimes.

2.3 Experimental procedure

All substrates listed in Table 1 and a reference smooth wall (SW) case were tested using the same procedure. The substrates were placed flush into the cutout and fluid was pumped through the test section. The flow rate was adjusted using the ball valve, beginning with the lowest measurable velocity and increased systematically in intervals until the maximum flow rate was reached. This was then repeated in the direction of decreasing flow rate. Approximately 50 points were collected for each flow rate. For each flow rate, a differential pressure transducer was used to measure the pressure difference between two ports for 30 seconds at a frequency of 4166 Hz after a 30-s settling period. Data were logged onto a PC workstation using a National Instruments data acquisition device. A pressure difference was measured at zero flow rate before and after each run to account for any zero offset in the transducer. The zero offset did not vary by more than 2% across all samples tested.

2.3.1 Identification of fully developed region

Based on established guidelines for the development of flow inside smooth wall ducts, the flow is considered fully developed at a distance of more than 50 times the hydraulic diameter ($\approx H_f$ in this case) (Byrne et al. 1969; Zanoun et al. 2009). However, there is limited information on development length over porous substrates. In previous experiments over anisotropic porous walls in a channel flow, Suga et al. (2017) conducted PIV experiments at $\approx 100H_f$ from the entrance and observed flow conditions that were fully developed for an aspect ratio of $W/H_f \approx 10$. On the other hand, Efstathiou and Luhar (2018) observed that flow can be considered fully developed over high-porosity isotropic foams in a flat-plate boundary layer at approximately $\approx 44H_p$ from the entrance. In the benchtop channel flow experiments performed by Chavarin et al. (2020) for $L/H_f \approx 30$, flow

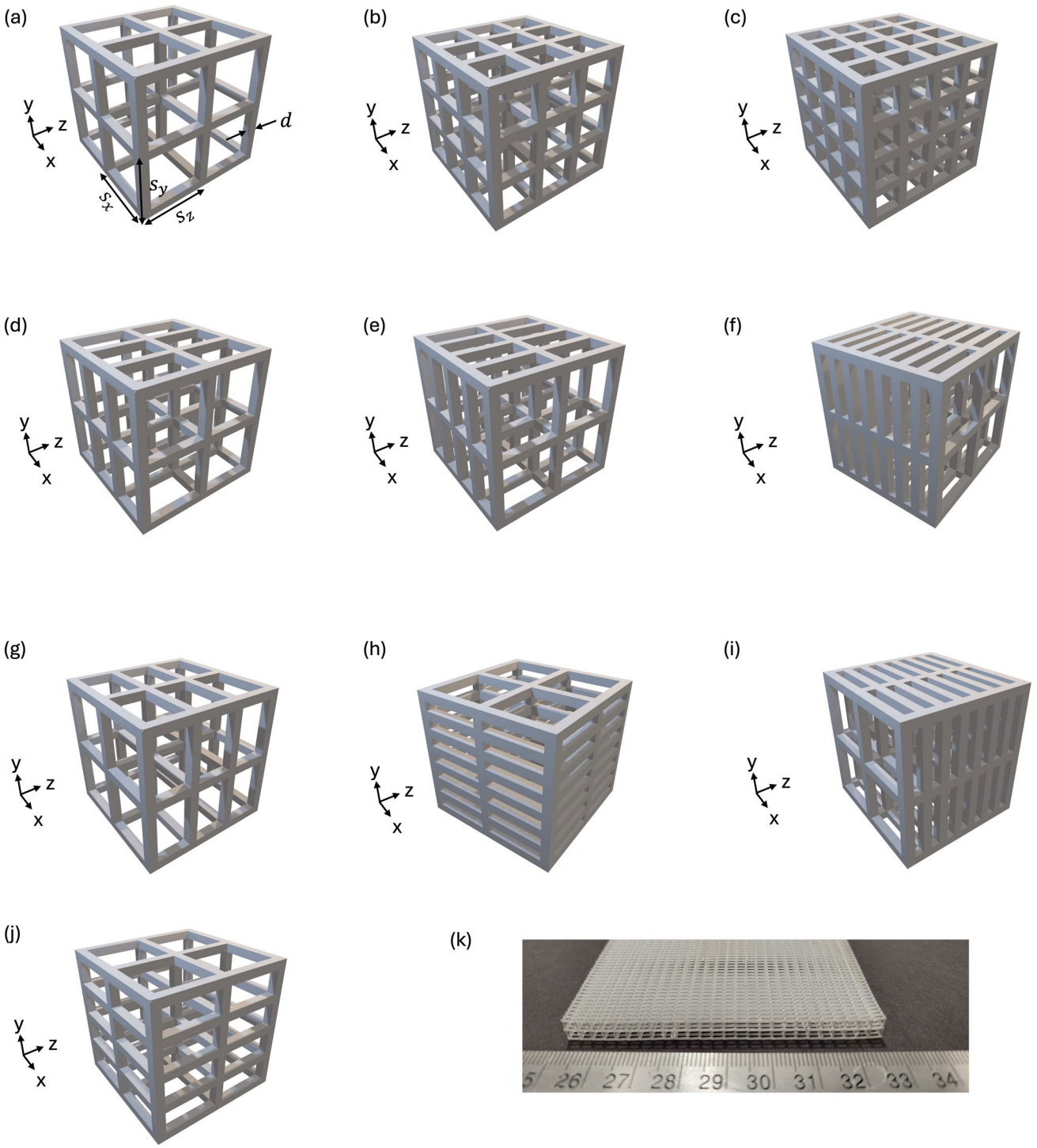

Fig. 2 Renderings of porous substrates: **a**, **b**, and **c** are the isotropic cases HHH, MMM, and LLL, respectively; **d**, **e**, and **f** depict MHH, LHH, and THH, where only the streamwise spacing s_x is varied; **f**, **h**, and **i** show rotated versions of the same nominal microstructure: THH, HTH, and HHT, respectively; **g** shows the HHM geometry, which is the rotated version of **d**; and **j** shows the HLH geometry, which is the rotated version of **e**. An image of a 3D printed porous tile is shown in panel **k**

Table 1 Parameter space used for the experiments

	d (mm)	s_x (mm)	s_y (mm)	s_z (mm)	$\kappa_{xx} \times 10^2$ (mm^2)	$\kappa_{yy} \times 10^2$ (mm^2)	$\kappa_{zz} \times 10^2$ (mm)^2	Marker
HHH	0.4	3	3	3	80 ± 20	80 ± 20	80 ± 20	○
	(0.49 ± 0.12)	(3.06 ± 0.28)	(2.98 ± 0.26)	(3.1 ± 0.26)				
MMM	0.4	2	2	2	10.4 ± 0.15	10.4 ± 0.15	10.4 ± 0.15	○
	(0.44 ± 0.04)	(1.86 ± 0.13)	(1.89 ± 0.12)	(1.88 ± 0.12)				
LLL	0.4	1.5	1.5	1.5	8.0 ± 1.2	8.0 ± 1.2	8.0 ± 1.2	○
	(0.48 ± 0.07)	(1.56 ± 0.17)	(1.63 ± 0.17)	(1.51 ± 0.17)				
MHH	0.4	2	3	3	7.3 ± 0.5	7.1 ± 0.5	7.1 ± 0.5	△
	(0.43 ± 0.03)	(2.09 ± 0.11)	(3.00 ± 0.08)	(2.96 ± 0.08)				
LHH	0.4	1.5	3	3	9.9 ± 0.9	3.6 ± 0.5	3.6 ± 0.5	△
	(0.37 ± 0.07)	(1.5 ± 0.2)	(2.9 ± 0.2)	(2.8 ± 0.2)				
THH	0.4	0.8	3	3	12.6 ±4.5	0.44±0.08	0.44±0.08	△
	(0.44 ± 0.11)	(0.84 ± 0.09)	(3.02 ± 0.10)	(3.09 ± 0.10)				
HHM	0.4	3	3	2	7.1 ± 0.5	7.1 ± 0.5	7.3 ± 0.5	◇
	(0.43 ± 0.03)	(2.96 ± 0.08)	(3.00 ± 0.08)	(2.09 ± 0.11)				
HHT	0.4	3	3	1.5	0.44±0.08	0.44±0.08	12.6 ±4.5	◇
	(0.44 ± 0.11)	(3.09 ± 0.10)	(3.02 ± 0.10)	(0.84 ± 0.09)				
HLH	0.4	3	1.5	3	3.6 ± 0.5	9.9 ± 0.9	3.6 ± 0.5	∗
	(0.45 ± 0.03)	(3.02 ± 0.08)	(1.51 ± 0.09)	(3.06 ± 0.09)				
HTH	0.4	3	0.8	3	0.44±0.08	12.6 ±4.5	0.44±0.08	∗
	(0.44 ± 0.04)	(3.09 ± 0.11)	(0.87 ± 0.09)	(3.09 ± 0.09)				

For the dimensions, the first row indicates the nominal sizes, while the values in parentheses show measured sizes for the 3D printed materials

appeared to be fully developed within the PIV window toward the trailing edge of the channel.

In this experiment, the flow was not tripped and instead allowed to develop naturally in the test section. However, it is possible that the transition from the upstream contraction to the test section with smooth or porous inserts may effectively act as a trip. Experiments were carried out to identify the region of the test section for which the flow can be considered fully developed while ensuring that the pressure gradient can be measured with reasonable experimental uncertainty. To determine an appropriate measurement region, a pressure difference was measured between the pressure port closest to the exit (port 7) and all other ports for a reference smooth wall at bulk Reynolds number $\mathrm{Re}_b = 2200$, which was used to estimate a pressure gradient dP/dx (see Fig. 1). Note that the use of a differential pressure transducer aided in limiting the uncertainty in the pressure gradient and friction factor estimates. Given the small-scale nature of the experimental setup (necessitated by 3D printing), the differences in absolute pressure along the channel are small. The use of absolute pressure transducers would have required the evaluation of these small differences between relatively large pressure values and hence result in an increased uncertainty.

In Fig. 3, 1–7 represents the pressure gradient measured between pressure port 1 and pressure port 7, 2–7 represents the pressure gradient measured between ports 2 and 7, and

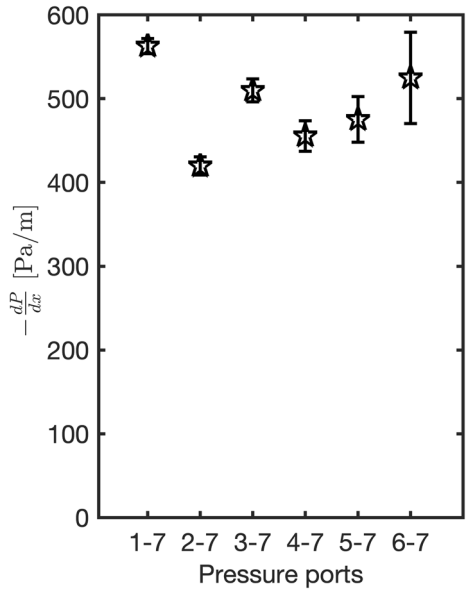

Fig. 3 Variation of pressure gradient $-dP/dx$ over a smooth wall measured between different pressure ports at $\mathrm{Re}_b = 2200$

so on. There is a noticeable variation in pressure gradient between 1–7, 2–7, and 3–7. However, for ports 4–7, 5–7, and 6–7, the measured pressure gradient converges within uncertainty. Note that the pressure gradient between 6–7 has relatively high measurement uncertainties due to the smaller

pressure drop expected between closely placed ports. Port 4 is located approximately $60H_f$ downstream of the entrance. This provides a sufficient development length based on guidelines presented in previous literature and is double the development length of Chavarin et al. (2020). Hence, all subsequent pressure gradients reported in this paper are based on pressure differences measured between pressure port 4 and pressure port 7.

2.3.2 Uncertainty quantification

There are two main sources of uncertainty for the friction factor measurements: pressure drop and flow rate measurements. To determine the uncertainty in mean pressure transducer measurements, we used the maximum of two values: (1) the standard error of each 30-second test run, consisting of over 120,000 samples taken at 4166 Hz and (2) the maximum uncertainty of the pressure transducer PX-409, which is 5.5 Pa. For each run, the uncertainty in flow rate measurement was 2%. Using the standard Klein–McClintock method for uncertainty propagation (Taylor and Thompson 1982), we estimated the absolute uncertainty in friction factor. Per Eq. (3), the friction factor estimates scale as $f \propto H_f^3$ since the height of the fluid domain is also used to estimate the bulk velocity U_b. Given this cubic dependence, uncertainty in H_f can contribute substantially to uncertainty in the friction factor estimate. However, since the channel was precision milled (tolerance $< 30\ \mu$m) and the 3D printed tiles were generated with a fine layer depth of 25 μm, we expect a maximum error of less than 1% in H_f. Independent measurements of the tile height (H_p) confirmed that the variation was less than 1%. Additionally, there is a significant source of error due to the deviation of desired microstructure dimensions for the 3D printed materials from the designed values, as shown in Table 1. Experimentally measured permeability estimates can be used to account for this.

3 Results and discussion

3.1 Smooth wall reference measurement

To obtain a reference measurement, a smooth solid wall was placed flush into the cutout. Figure 4 shows the measured pressure gradient for the smooth wall at various values of bulk averaged velocity. The flow transitions from laminar flow across the range of velocities tested, as evidenced by the linear region in the pressure gradient below $U_b \approx 0.2$ m/s ($\mathrm{Re}_b \approx 1600$) and a near-quadratic trend beyond this value. The pressure gradient is used to compute the Darcy–Weisbach friction factor:

$$f^* = -\frac{\mathrm{d}P}{\mathrm{d}x}\frac{2D_l}{\rho U_b^2}. \tag{1}$$

In this equation, the laminar equivalent diameter, D_l, is used as the characteristic length scale. The laminar equivalent diameter was proposed by Jones (1976) to ensure geometric similarity between circular and rectangular ducts. A modified Reynolds number Re_b^* is defined using this equivalent diameter to allow the relationship expected for laminar flow in smooth wall pipes with circular cross sections, $f_0^* = 64/\mathrm{Re}_b^*$, to be easily applied to duct flows with non-circular cross sections. For a rectangular duct of width W and height H_f, D_l is defined as follows:

$$D_l = \left(\frac{2}{3} + \frac{11}{24}\frac{H_f}{W}\left(2 - \frac{H_f}{W}\right)\right)D_h. \tag{2}$$

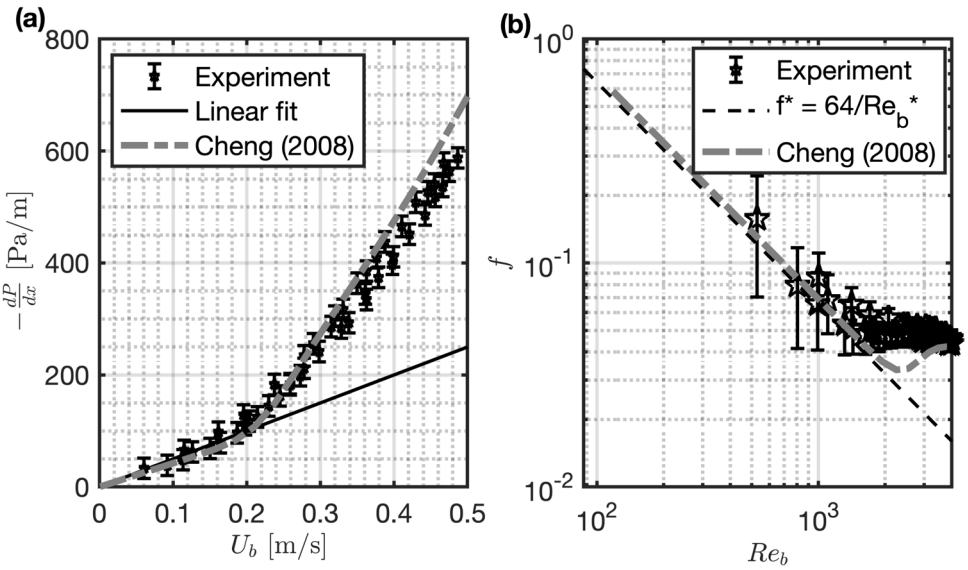

Fig. 4 **a** Variation of pressure gradient with bulk velocity for a smooth wall. **b** Variation of friction factor f^* with bulk Reynolds number compared with empirical predictions for a smooth laminar duct and the empirical correlation developed by Cheng (2008)

Here, $D_h = 4H_f W/2(H_f + W)$ is the hydraulic diameter.

Figure 4 compares friction factors estimated from the smooth wall pressure drop measurements against model predictions for f^*. For low Reynolds numbers, the measurements agree with the theoretical prediction $f_0^* = 64/\mathrm{Re}_b^*$ within uncertainty. The flow transitions for $\mathrm{Re}_b \gtrsim 1600$ and appears to become fully turbulent for $\mathrm{Re}_b \gtrsim 3000$. For these higher Re_b values, the friction factor asymptotes to a value that aligns well with the empirical correlation proposed by Cheng (2008). Together, these measurements confirm that the benchtop channel and pressure measurement system can reproduce prior results for smooth wall conditions.

3.2 Porous wall friction factor measurements

Each porous sample listed in Table 1 was flush-mounted into the cutout and the pressure gradient was measured across ports 4–7. A representative plot of the pressure gradient with bulk averaged velocity for the high-porosity isotropic case HHH is displayed in Fig. 5. The friction factor for each data point can be determined using the following equation:

$$f = -\frac{\mathrm{d}P}{\mathrm{d}x}\frac{2H_f}{\rho U_b^2}, \tag{3}$$

where the unobstructed channel height H_f is used as the characteristic length scale. We use this definition for all subsequent friction factor calculations as the laminar equivalent diameter is only applicable to channel flow with smooth walls; its validity for porous walls is uncertain. Friction factor estimates generated using H_f as the characteristic length scale are presented without the $()^*$ superscript.

For lower values of Re_b, the flow is expected to be laminar and the pressure gradient is expected to scale linearly with bulk velocity, $\mathrm{d}P/\mathrm{d}x \sim U_b$. At higher Re_b values, the pressure gradient is expected to show a quadratic dependence, $\mathrm{d}P/\mathrm{d}x \sim U_b^2$.

This is evident in Fig. 5b, which shows that there is a linear relationship between $-\frac{1}{U_b}\frac{\mathrm{d}P}{\mathrm{d}x}$ and U_b with the constants a and b representing the slope and the intercept:

$$-\frac{1}{U_b}\frac{\mathrm{d}P}{\mathrm{d}x} = aU_b + b. \tag{4}$$

We can combine Eq. (3) with (4) to show that

$$f = \frac{2H_f}{\rho}\left(a + \frac{b}{U_b}\right) = C_1 + \frac{C_2}{\mathrm{Re}_b} \tag{5}$$

where $C_1 = 2H_f a/\rho$ is an estimate for the asymptotic value of the Darcy–Weisbach friction factor for large Re_b. The second term C_2/Re_b represents the initial (laminar) relationship between pressure drop and bulk velocity, with $C_2 = 2H_f^2 b/\mu$.

Figure 6 compares the pressure gradient and the friction factor for isotropic, high-spacing HHH case with the reference smooth wall (SW) measurement. HHH consistently shows a pressure gradient that is approximately twice as large as that for SW. This translates into a higher friction factor value for each Reynolds number. Note that the shaded region in Fig. 6 represents the 95% confidence interval for the friction factor obtained by the curve fit. Here, H_f is used as the characteristic length scale for both HHH and SW to ensure consistency. Measurements for the remaining isotropic and anisotropic porous foams are discussed in the following subsections. For clarity, only the curve fits (with 95% confidence intervals) are shown.

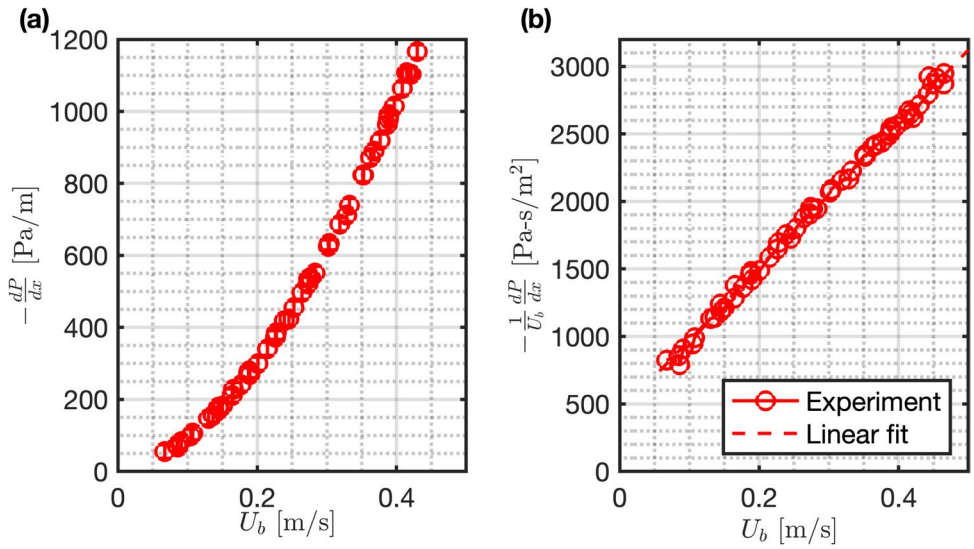

Fig. 5 **a** Variation of pressure gradient with bulk velocity for HHH. **b** Transformation showing linear fitting procedure to estimate the value of friction factor

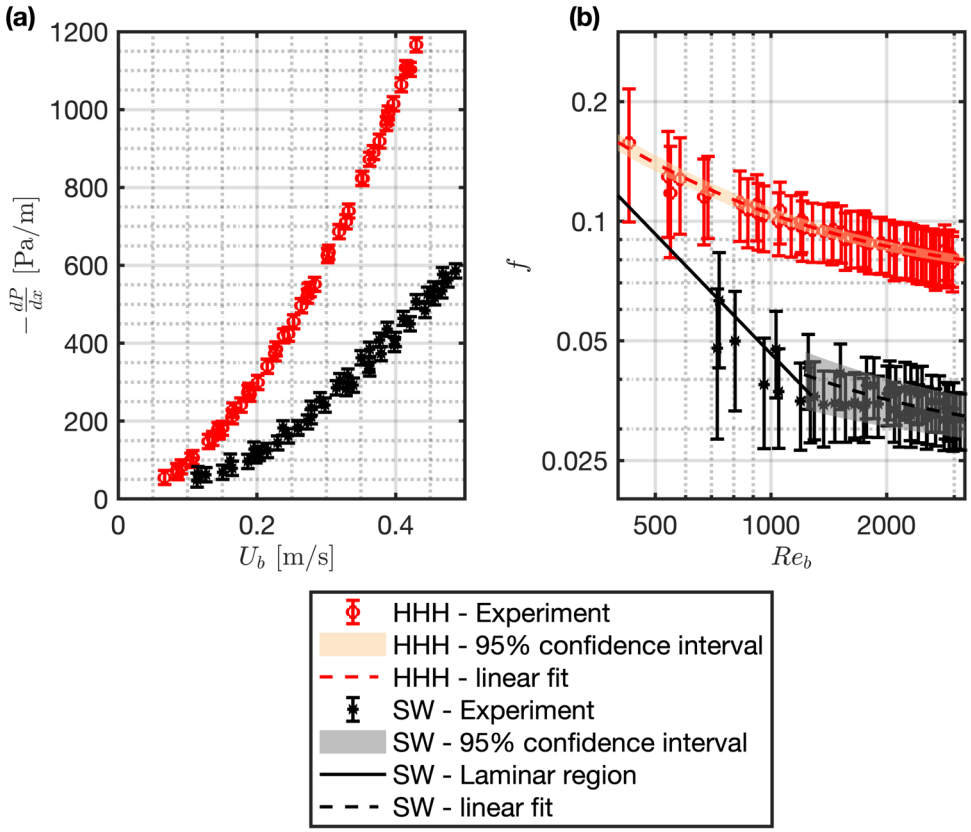

Fig. 6 **a** Pressure gradient measurements for HHH and smooth wall (SW) reference. **b** Friction factor estimates for HHH and SW cases

3.3 Observations over isotropic substrates

Figure 7a illustrates the changes in friction factor with bulk Reynolds number for all isotropic permeability cases (HHH, MMM, LLL) in comparison with smooth wall values. As the Reynolds number decreases, all three cases reach a state of laminar behavior. However, all cases show a deviation from laminar values at Reynolds numbers lower than the smooth wall, which is indicative of an earlier transition to turbulence. HHH and MMM consistently generate higher friction factors than LLL for all tested Reynolds numbers. Thus, for these isotropic cases, an increase in permeability leads to higher drag for a given Reynolds number.

Note that the rod spacing varies from 1.5 mm (LLL) to 3.0 mm (HHH) for the isotropic substrates. As the substrate pore size (and hence permeability) increases, the ratio of substrate thickness to pore size (H_p/s) approaches unity. For the largest pore sizes considered here (e.g., case HHH), the pore-scale Reynolds number is large: $s^+ = \frac{u_\tau s}{\nu} > 40$, where u_τ is an *average* friction velocity estimated from a simplified momentum balance of the form $2\rho u_\tau^2 \approx -\frac{\mathrm{d}P}{\mathrm{d}x} H_f$. Thus, there is limited separation between the pore scale and the outer length scale (i.e., for s comparable to $H_f = H_p$) in the flow and the substrate essentially acts as a layer of drag-producing large-scale roughness.

3.4 Observations over anisotropic substrates

Figure 7b shows that the friction factor curves for HHH, MHH, and LHH approximately converge for high Reynolds numbers. However, as the streamwise spacing is reduced further, for case THH the friction factor curve is significantly lower than the curves for the remaining anisotropic materials and is only marginally higher than the SW reference case. In other words, substrate THH generates significantly lower drag compared to the LHH, MHH, and HHH substrates. Decreasing s_x restricts the pore size in the wall-normal and spanwise directions, i.e., reduces κ_{yy} and κ_{zz}, while approximately maintaining κ_{xx}. Therefore, THH is the most streamwise-preferential material (i.e., the material with the highest anisotropy ratio ϕ_{xz}) and shows the smallest drag increase. For LHH and MHH, an increase in s_x leads to an increase in κ_{yy} and κ_{zz}.

Despite being streamwise preferential, the THH material does not yield drag reduction. This is consistent with previous observations made in experiments utilizing similar porous materials to the THH case (Chavarin et al. 2020), where no drag reduction was observed compared to a smooth wall. The increase in drag for the THH case could be potentially due to two causes. First, the wall-normal permeability scale $\sqrt{\kappa_{yy}}^+$ is greater than the thresh-

old for the emergence of KH rollers (Gómez-De-Segura and García-Mayoral 2019). This effect is considered below. Second, the geometry at the interface consists of a thick layer of spanwise-oriented horizontal rods (see Fig. 2f), which is likely to restrict the effective mean slip length, ℓ_U^+, that is essential for drag reduction. Indeed, the results show a minimal drag penalty associated with rotating the THH microstructure by 90 deg around the wall-normal axis to yield the HHT case with spanwise-preferential permeability (see Table 2). This is because the rotated microstructure (Fig. 2h) has slots oriented in the streamwise direction, which may yield improved streamwise slip, but maintains low wall-normal permeability.

These results are broadly consistent with prior experimental efforts and DNS simulations employing the same cubic lattice geometry (Chavarin et al. 2020; Efstathiou and Luhar 2020; Habibi Khorasani et al. 2024), which do not show drag reduction for streamwise-preferential materials. As noted earlier the presence of the spanwise-oriented rods limits interfacial slip and leads to a decorrelation between the streamwise permeability and slip.

Now consider Fig. 7c, where we vary spacing in the spanwise direction. This figure shows that the HHT material generates lower drag than the HHM and HHH materials, which have larger values for the spanwise spacing s_z. Limiting s_z results in limiting pore size for wall-normal and streamwise flow. Consequently, HHT has the lowest κ_{xx} and κ_{yy} of the materials considered in this figure. In principle, a low value of κ_{xx} is not a preferable configuration to reduce drag. However, a low value of $\sqrt{\kappa_{yy}}^+$ limits

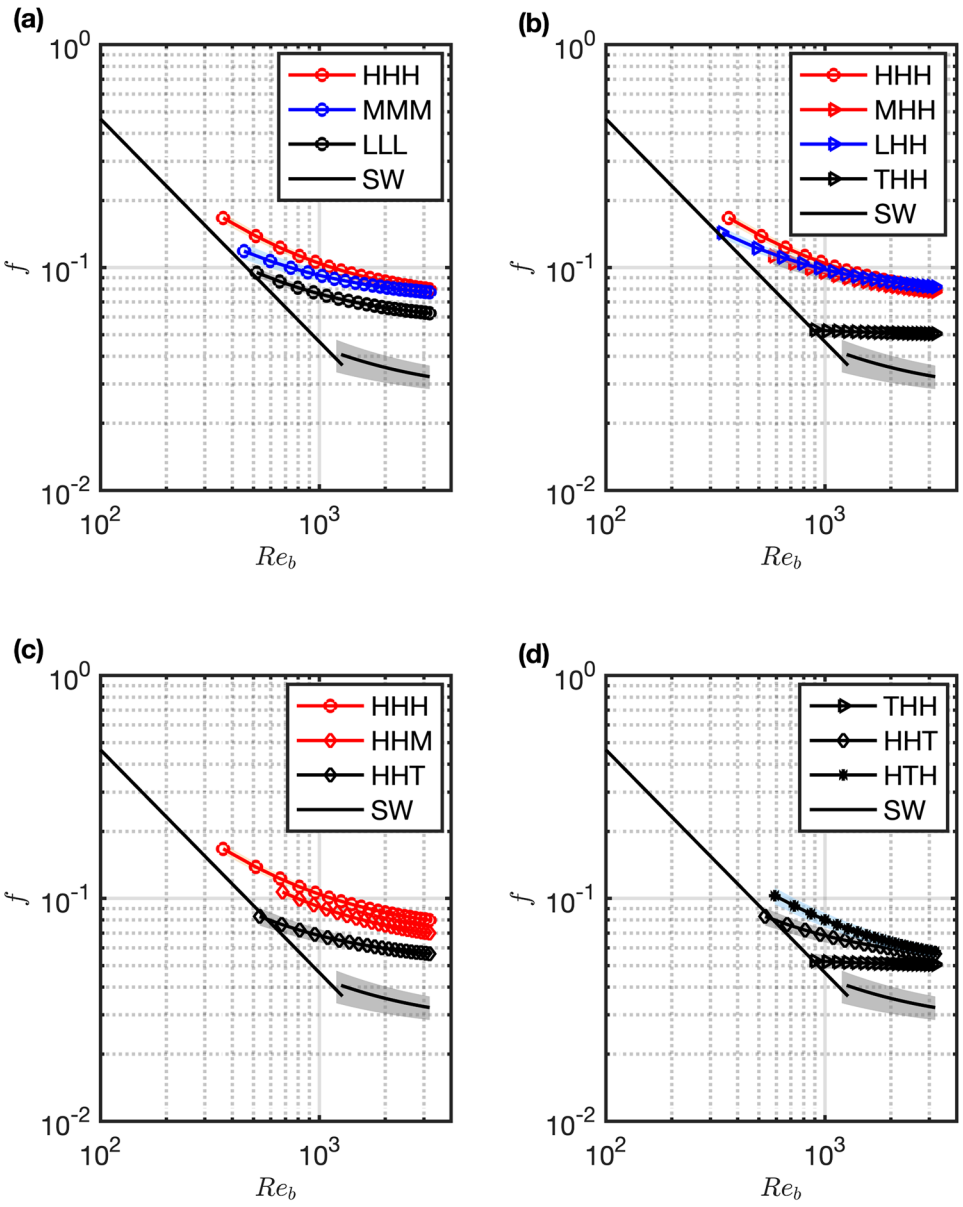

Fig. 7 Friction factor measurements for **a** isotropic geometries, **b** varying rod spacings in x, **c** varying rod spacings in z, and **d** varying microstructure orientation

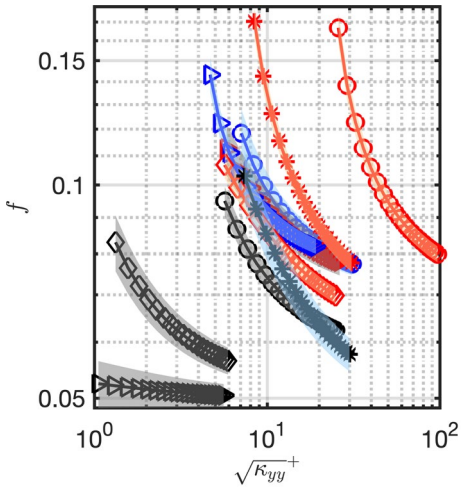

Fig. 8 Friction factor f plotted against inner-normalized permeability length scale $\sqrt{\kappa_{yy}}^+$ for all porous substrates. For the legend, see Table 1

Table 2 Values of a and b as estimated from the linear curve fitting process for each tile, see (4)

	$a(\div 10^3)$	$b(\div 10^3)$	C_1	$\hat{\mathrm{Re}}_b$
HHH	5.37	0.44	6.3×10^{-2}	540
MMM	5.6	0.0.27	6.5×10^{-2}	730
LLL	4.38	0.25	5.5×10^{-2}	900
MHH	5.49	0.30	6.2×10^{-2}	690
LHH	5.83	0.29	6.7×10^{-2}	630
THH	3.89	0.03	4.3×10^{-2}	1370
HHM	4.67	0.39	6.0×10^{-2}	680
HHT	4.00	0.21	4.5×10^{-2}	1100
HLH	5.00	0.54	6.4×10^{-2}	410
HTH	3.70	0.40	4.8×10^{-2}	800

As Re_b increases, f asymptotes to $C_1 = 2aH_f/\rho$ per (5). To estimate the Reynolds number at which flow has transitioned from the laminar regime, we use $\hat{\mathrm{Re}}_b = 1.5 f_s$, where f_s is the laminar smooth wall friction factor

the drag penalty. Moreover, as noted above, for small s_z and large s_x values, the dense upper layer of rods is aligned in the direction of the flow, which may be beneficial for the interfacial slip.

We can observe the effect of microstructure orientation on the drag response in Fig. 7d. The streamwise-preferential material (THH with $\kappa_{xx} > \kappa_{yy} = \kappa_{zz}$) has the lowest drag penalty, as expected. HHT follows with the next best performance, likely due to its low κ_{yy}. The HTH case experiences the greatest drag increase, which is mainly attributed to its large s_x and s_z and thus large openings for the wall-normal flow (large $k_y y$), which is known to be detrimental for drag.

Figure 8 further illustrates the effect of the wall-normal permeability $\sqrt{\kappa_{yy}}^+ = \sqrt{\kappa_{yy}} u_\tau/\nu$. For all porous substrates and Re_b values tested, the inner-normalized permeability is $\sqrt{\kappa_{yy}}^+ > 1$. This is greater than the threshold identified in previous literature for the emergence of spanwise rollers, $\sqrt{\kappa_{yy}}^+ \approx 0.4$, which are known to compromise drag reduction performance. As before, to calculate $\sqrt{\kappa_{yy}}^+ = \frac{u_\tau \sqrt{\kappa_{yy}}}{\nu}$, we estimate u_τ based on a simplified momentum balance in the unobstructed channel: $2\rho u_\tau^2 = -\frac{\mathrm{d}P}{dx} H_f$. The pressure drop and friction factor measurements presented here indicate no evidence of drag reduction compared to the smooth wall values. Based on these observations, it may be the case that all the porous substrates considered here are susceptible to the emergence of spanwise rollers. This is consistent with DNS observations (Habibi Khorasani et al. 2024) which show pronounced increases in Reynolds shear stress for substrates with $\sqrt{\kappa_{yy}}^+ > 1$, resulting in increased drag ($\Delta U^+ < 0$). In general, samples with a higher κ_{yy}, and hence a higher $\sqrt{\kappa_{yy}}^+$, show a higher friction factor.

3.5 Departure from laminar regime

There has been a sustained effort to model the onset of transition over rough walls. Tools such as the Moody diagram provide consolidated results that can be used by practitioners. However, currently there is limited information available regarding the onset of transition over porous walls. Suga et al. (2010) have demonstrated that increasing wall permeability for stochastic isotropic foams increases turbulence, and generally leads to a lower Reynolds number for transition.

Recent experiments in an asymmetric channel configuration testing high-porosity ($\epsilon = 0.7$) anisotropic porous materials made of layered meshes (Suga et al. 2018) show that the mean velocity profile remains parabolic at $\mathrm{Re}_b = 900$. Complete transition to turbulence occurs at $\mathrm{Re}_b = 3600$ for materials with a permeability ratio $\phi_{xy} = \kappa_{xx}/\kappa_{yy} \approx 0.006$. For two other cases with higher streamwise permeability, $\phi_{xy} \approx 0.67$ and $\phi_{xy} \approx 0.84$, the flow transitions to turbulence earlier at $\mathrm{Re}_b < 3400$. This suggests that for materials with high wall-normal permeability ($\phi_{xy} < 1$), an increase in streamwise permeability may allow wall-penetrating vortices to better maintain their strength. This could trigger an earlier transition to turbulence. In this sense, the anisotropy ratio influences transition. Of course, the actual pore size also plays a critical role in dictating transition since it sets the effective roughness.

The friction factor data obtained in this study fall within the range of $500 < \mathrm{Re}_b < 4000$. As shown in Fig. 7, the fitted friction factor curves asymptotically approach the laminar smooth wall curve for nearly all the materials tested as Re_b decreases to below 500. For some materials (e.g., THH), the measured friction factors approach the laminar SW curve earlier as Re_b decreases. For high Re_b values, the friction

factor data asymptote toward a constant value that is higher than the smooth wall reference. This is representative of the fully rough regime. Per Eq. (5), for $\mathrm{Re}_b \gg C_2$, we expect $f \to C_1 = 2aH_f/\rho$. Estimated values for this asymptotic limit for the friction factor are shown in Table 2.

We generate an approximate estimate for the Reynolds number, $\hat{\mathrm{Re}}_b$, at which flow over the porous walls transitions away from laminar regime and toward turbulence. Specifically, we identify the threshold for which $f > 1.5f_s$, where f_s represents the laminar smooth wall friction factor. Estimated values for $\hat{\mathrm{Re}}_b$ are listed in Table 2. Though $1.5f_s$ is an arbitrary cutoff, the $\hat{\mathrm{Re}}_b$ estimates show trends consistent with expectation. Specifically, cases THH and HHT which have the lowest wall-normal permeability show the highest $\hat{\mathrm{Re}}_b$, i.e., the transition occurs later for these low κ_{yy} cases. We estimate $\hat{\mathrm{Re}}_b = 1370$ for case THH and $\hat{\mathrm{Re}}_b = 1100$ for case HHT. Note that these values are both below the threshold observed for the reference smooth wall measurement, $\hat{\mathrm{Re}}_b \approx 1600$. The earliest transition is observed for the high-permeability HLH ($\hat{\mathrm{Re}}_b = 410$) and HHH ($\hat{\mathrm{Re}}_b = 540$) cases. This is broadly consistent with previous studies that show an earlier transition to turbulence for high-permeability foams (Suga et al. 2010).

Interestingly, the case HLH yields a lower $\hat{\mathrm{Re}}_b$ value compared to the case HHH, which has the highest permeability (see Table 1). At first glance, this is inconsistent with the findings of Suga et al. (2018) which suggest that, for materials with high wall-normal permeability, an increase in streamwise permeability can trigger an earlier transition to turbulence. Physically, the high streamwise permeability can permit fluctuations more freely in the porous domain. The materials tested by Suga et al. (2018) had anisotropy ratios of $\phi_{xy} \approx 0.006$, 0.67 and 0.84. The latter two materials exhibited an earlier transition to turbulence. For the materials with high wall-normal permeability considered here, the anisotropy ratios are $\phi_{xy} \approx 0.035$ (Case HTH), 0.36 (Case HLH), and 1 (Case HHH). Per the estimates in Table 2, these materials show departure from the laminar smooth wall curve for $\hat{\mathrm{Re}}_b \approx 800$ (Case HTH), 410 (Case HLH), and 540 (Case HHH). Thus, the initial increase in streamwise permeability from Case HTH to Case HLH does trigger transition earlier which is consistent with the findings of Suga et al. (2018). However, the subsequent increase in streamwise permeability from Case HLH to Case HHH delays transition. This non-monotonic behavior may reflect a competition between different physical mechanisms. While high streamwise permeability for Case HHH can allow increased turbulent fluctuations in the porous domain, the mean profile for Case HLH may exhibit greater shear near the interface. Increased interfacial shear, coupled with high wall-normal permeability may trigger an earlier transition to turbulence via an interfacial instability mechanism.

4 Conclusion

This effort presents the first dataset of measurements of friction factor over a wide range of anisotropy for physically realizable (3D printed) porous materials. Previous experiments and numerical simulations have suggested the use of streamwise-preferential substrates for drag reduction. Models developed in these prior studies indicate that materials with high streamwise permeability and low spanwise permeability are promising candidates for passive drag reduction, while high wall-normal permeabilities compromise performance by triggering rollers resembling Kelvin–Helmholtz (KH) vortices. However, prior numerical simulations have primarily considered low to moderate Reynolds numbers and used the idealized Darcy–Brinkman equation in the porous medium. Similarly, prior experimental datasets are limited in that friction velocities are not directly obtained from an independent measure but inferred from other turbulent quantities such as Reynolds shear stress measurements. Moreover, there are few experimental datasets available that systematically examine the impact of anisotropic porous materials on drag. This effort addresses this limitation by leveraging 3D printing techniques to create a family of anisotropic materials and generates direct drag estimates for these materials via pressure drop measurements.

For isotropic substrates, an increase in permeability (or pore size) leads to higher drag for a given Reynolds number. At the large pore limit, the substrate acts as a layer of drag-producing large-scale roughness with limited separation between the pore scale and the outer length scale in the flow. While we do not observe drag reduction, porous substrates with high streamwise permeability and low spanwise and wall-normal permeabilities resulted in the smallest drag increment compared to a reference smooth wall measurement. Specifically, the THH material is perhaps the most "streamwise-preferential" case considered here (nominal $\phi_{xz} > 25$) and shows the smallest increase in drag. For the other streamwise-preferential cases LHH and MHH, an increase in the streamwise spacing s_x leads to an increase in κ_{yy} and κ_{zz}. These materials further increase drag compared to a smooth wall.

We estimate that the wall-normal permeabilities for all tested cases exceeded the threshold ($\sqrt{\kappa_{yy}}^{+} > 0.4$) for the emergence of energetic spanwise rollers similar to KH vortices. This is consistent with the result that drag reduction was not observed in the current dataset. In addition, the specific interfacial geometry is also likely to play a role by decreasing the effective slip length for the streamwise mean flow. Our measurements indicate that porous walls exhibit a departure from laminar behavior at different values for bulk Reynolds numbers depending on the geometry. Streamwise-preferential materials depart from smooth

wall behavior at higher values for bulk Reynolds number. Materials with the highest wall-normal permeabilities exhibited departure from smooth wall behavior at the lowest Re_b values.

The findings indicate that streamwise-preferential porous materials could be a viable solution to reduce drag in turbulent wall-bounded flows—or minimize the drag penalty for other applications such as thermal management and noise or signature reduction. It is important to be mindful, however, that the chosen interfacial geometry should not lead to a decrease in slip. Additionally, when the relative foam thickness is $h/s \sim O(1)$, roughness and inertial effects may contribute to an increase in friction. Future particle image velocimetry experiments are planned to measure the mean profile, turbulence statistics to isolate the roughness function and potentially document the existence of the Kelvin–Helmholtz vortices.

Acknowledgements We would like to acknowledge the support of the Air Force Office of Scientific Research under award FA9550-19-1-7027, with program managers D. Smith and G. Abate and the National Science Foundation grant no. 1943105. We are also grateful to Idan Eizenberg and Sonal Sukhatme for their contributions in taking permeability measurements, and to Dr. Christoph Efstathiou for designing the benchtop channel. This work benefited from collaborative discussions with Seyed Khorasani and Dr. Shervin Bagheri from the KTH Royal Institute of Technology. We are also grateful for the valuable inputs provided by Sasindu Pinto and Dr. Louis Cattafesta from the Illinois Institute of Technology.

Author contributions S.V. and M.L. conceptualized the research project and planned the experimental work. S.V. designed and performed the experiments, processed the data, and prepared the figures and the original draft of the manuscript. M.L. reviewed and edited the manuscript and secured funding and the resources for the study.

Funding Open access funding provided by SCELC, Statewide California Electronic Library Consortium. We would like to acknowledge the support of the Air Force Office of Scientific Research under award FA9550-19-1-7027, with program managers D. Smith and G. Abate and the National Science Foundation grant no. 1943105.

Data availability Data are available upon request.

Declarations

Conflict of interest The authors declare no competing interests.

Ethical approval Not applicable.

References

Abderrahaman-Elena N, García-Mayoral R (2017) Analysis of anisotropically permeable surfaces for turbulent drag reduction. Phys Rev Fluids. https://doi.org/10.1103/PhysRevFluids.2.114609

Boomsma K, Poulikakos D (2002) The effects of compression and pore size variations on the liquid flow characteristics in metal foams. J Fluids Eng, Trans ASME 124(1):263–272. https://doi.org/10.1115/1.1429637

Boomsma K, Poulikakos D, Zwick F (2003) Metal foams as compact high performance heat exchangers. Mech Mater 35(12):1161–1176. https://doi.org/10.1016/j.mechmat.2003.02.001

Breugem WP, Boersma BJ, Uittenbogaard RE (2006) The influence of wall permeability on turbulent channel flow. J Fluid Mech 562(9):35–72. https://doi.org/10.1017/S0022112006000887

Byrne J, Hatton A, Marriott P (1969) Turbulent flow and heat transfer in the entrance region of a parallel wall passage. Proc Inst Mech Eng 184(1):697–712

Chandesris M, D'Hueppe A, Mathieu B, Jamet D, Goyeau B (2013) Direct numerical simulation of turbulent heat transfer in a fluid-porous domain. Phys Fluids 25(12):125110. https://doi.org/10.1063/1.4851416

Chavarin A, Efstathiou C, Vijay S, Luhar M (2020) Resolvent-based design and experimental testing of porous materials for passive turbulence control. Int J Heat Fluid Flow 86:12. https://doi.org/10.1016/j.ijheatfluidflow.2020.108722

Cheng N-S (2008) Formulas for friction factor in transitional regimes. J Hydraul Eng 134(9):1357–1362

Choi H, Moin P, Kim J (1993) Direct numerical simulation of turbulent flow over riblets. J Fluid Mech 255:503–539. https://doi.org/10.1017/S0022112093002575

Clyne T, Golosnoy I, Tan J, Markaki A (2006) Porous materials for thermal management under extreme conditions. Philos Trans Royal Soc A: Math, Phys Eng Sci 364(1838):125–146

Efstathiou C, Luhar M (2018) Mean turbulence statistics in boundary layers over high-porosity foams. J Fluid Mech 841:351–379. https://doi.org/10.1017/jfm.2018.57

Efstathiou C, Luhar M (2020) Turbulent boundary layers over streamwise-preferential porous materials. URL arXiv:2006.00182

Endrikat S, Modesti D, García-Mayoral R, Hutchins N, Chung D (2021) Influence of riblet shapes on the occurrence of kelvin-helmholtz rollers. J Fluid Mech 913:A37

García-Mayoral R, Jiménez J (2011) Drag reduction by riblets. Philos Trans Royal Soc A: Math, Phys Eng Sci 369(1940):1412–1427. https://doi.org/10.1098/rsta.2010.0359

García-Mayoral R, Jiménez J (2011) Hydrodynamic stability and breakdown of the viscous regime over riblets. J Fluid Mech 678:317–347. https://doi.org/10.1017/jfm.2011.114

Gómez-De-Segura G, García-Mayoral R (2019) Turbulent drag reduction by anisotropic permeable substrates-analysis and direct numerical simulations. J Fluid Mech. https://doi.org/10.1017/jfm.2019.482

Habibi Khorasani SM, Luhar M, Bagheri S (2024) Turbulent flows over porous lattices: alteration of near-wall turbulence and pore-flow amplitude modulation. J Fluid Mech 984:A63. https://doi.org/10.1017/jfm.2024.198

Ibrahim JI, Ómez-de Segura GG, Chung D, García-Mayoral R (2021) The smooth-wall-like behaviour of turbulence over drag-altering surfaces: a unifying virtual-origin framework. J Fluid Mech 915:A56

Jaworski JW, Peake N (2013) Aerodynamic noise from a poroelastic edge with implications for the silent flight of owls. J Fluid Mech 723:456–479

Jaworski JW, Peake N (2020) Aeroacoustics of silent owl flight. Annu Rev Fluid Mech 52:395–420

Jones O (1976) An improvement in the calculation of turbulent friction in rectangular ducts. J Fluids Eng 98(2):173–180

Luchini P (1996) Reducing the turbulent skin friction. In: Computational methods in applied sciences' 96 (Paris, 9-13 September 1996), pp 465–470

Luchini P, Manzo F, Pozzi A (1991) Resistance of a grooved surface to parallel flow and cross-flow. J Fluid Mech 228:87–109. https://doi.org/10.1017/S0022112091002641

Morimoto M, Aoki R, Kuwata Y, Suga K (2023) Measurements for characteristics of turbulence over a streamwise preferential porous substrate. Flow Turbul Combust. https://doi.org/10.1007/s10494-023-00493-4

Robinson SK (1991) Coherent motions in the turbulent boundary layer. Annu Rev Fluid Mech 23(1):601–639

Suga K, Matsumura Y, Ashitaka Y, Tominaga S, Kaneda M (2010) Effects of wall permeability on turbulence. Int J Heat Fluid Flow 31(6):974–984. https://doi.org/10.1016/j.ijheatfluidflow.2010.02.023

Suga K, Nakagawa Y, Kaneda M (2017) Spanwise turbulence structure over permeable walls. J Fluid Mech 822:186–201. https://doi.org/10.1017/jfm.2017.278

Suga K, Okazaki Y, Ho U, Kuwata Y (2018) Anisotropic wall permeability effects on turbulent channel flows. J Fluid Mech 855:983–1016. https://doi.org/10.1017/jfm.2018.666

Taylor JR, Thompson W (1982) An introduction to error analysis: the study of uncertainties in physical measurements, vol 2. Springer, Berlin

Walsh M (1982) Turbulent boundary layer drag reduction using riblets. In: Aerospace Sciences Meeting. American Institute of Aeronautics and Astronautics (AIAA). https://doi.org/10.2514/6.1982-169

Zanoun ES, Kito M, Egbers C (2009) A study on flow transition and development in circular and rectangular ducts. J Fluids Eng, Trans ASME 131(6):0612041–06120410. https://doi.org/10.1115/1.3112384